OPEN ACCESS
IOP Publishing | National Institute for Materials Science
Science and Technology of Advanced Materials
Sci. Technol. Adv. Mater. **15** (2014) 035015 (13pp)
doi:10.1088/1468-6996/15/3/035015

Drastic influence of minor Fe or Co additions on the glass forming ability, martensitic transformations and mechanical properties of shape memory Zr–Cu–Al bulk metallic glass composites

Sergio González[1], Pablo Pérez[2], Emma Rossinyol[3], Santiago Suriñach[1], Maria Dolors Baró[1], Eva Pellicer[1] and Jordi Sort[4]

[1] Departament de Física, Facultat de Ciències, Universitat Autònoma de Barcelona, E-08193 Bellaterra, Spain
[2] Departamento de Metalurgia Física, Centro Nacional de Investigaciones Metalúrgicas, CENIM, CSIC, Avda. Gregorio del Amo 8, E-28040 Madrid, Spain
[3] Servei de Microscòpia, Universitat Autònoma de Barcelona, E-08193 Bellaterra, Spain
[4] Institució Catalana de Recerca i Estudis Avançats (ICREA) and Departament de Física, Universitat Autònoma de Barcelona, E-08193 Bellaterra, Spain

E-mail: Sergio.Gonzalez@uab.cat and Jordi.Sort@uab.cat

Received 2 February 2014
Accepted for publication 5 June 2014
Published 27 June 2014

Abstract

The microstructure and mechanical properties of $Zr_{48}Cu_{48-x}Al_4M_x$ (M ≡ Fe or Co, $x = 0$, 0.5, 1 at.%) metallic glass (MG) composites are highly dependent on the amount of Fe or Co added as microalloying elements in the parent $Zr_{48}Cu_{48}Al_4$ material. Addition of Fe and Co promotes the transformation from austenite to martensite during the course of nanoindentation or compression experiments, resulting in an enhancement of plasticity. However, the presence of Fe or Co also reduces the glass forming ability, ultimately causing a worsening of the mechanical properties. Owing to the interplay between these two effects, the compressive plasticity for alloys with $x = 0.5$ (5.5% in $Zr_{48}Cu_{47.5}Al_4Co_{0.5}$ and 6.2% in $Zr_{48}Cu_{47.5}Al_4Fe_{0.5}$) is considerably larger than for $Zr_{48}Cu_{48}Al_4$ or the alloys with $x = 1$. Slight variations in the Young's modulus (around 5–10%) and significant changes in the yield stress (up to 25%) are also observed depending on the composition. The different microstructural factors that have an influence on the mechanical behavior of these composites are investigated in detail: (i) co-existence of amorphous and crystalline phases in the as-cast state, (ii) nature of the crystalline phases (austenite versus martensite content), and (iii) propensity for the austenite to undergo a mechanically-driven martensitic transformation during plastic deformation. Evidence for intragranular nanotwins likely generated in the course of the austenite–martensite transformation is provided by transmission electron microscopy. Our results reveal that fine-tuning of the composition of the Zr–Cu–Al–(Fe,Co) system is crucial in order to optimize the

mechanical performance of these bulk MG composites, to make them suitable materials for structural applications.

Keywords: metallic glass, composite, shape memory alloy, plasticity, nanoindentation, martensitic transformation, Cu–Zr–Al–(Fe, Co)

1. Introduction

Metallic glasses (MGs) are an interesting class of materials with outstanding mechanical properties, such as high elastic strain and large hardness [1, 2]. However, their use for structural applications remains rather limited because of their poor ductility at room temperature, which stems from localization of plastic flow in discrete shear bands, whose rapid propagation causes premature fracture [3, 4]. This drawback can be overcome, to some extent, by designing MG composites with second-phase particles embedded in the glassy matrix. Such particles introduce stress concentrations that promote nucleation and branching of shear bands. At the same time, these particles can also disrupt catastrophic shear propagation if their size is larger than the thickness of shear bands (10–100 nm) [3]. Actually, both the size and the shape of the second-phase particles are important in order to hinder shear band propagation. A dendritic morphology appears to be the most effective shape to arrest shear bands [2].

Recent studies have shown that MG composites can attain even larger plasticity when the second-phase particles consist of a shape memory alloy [5]. These composites combine the high strength and hardness of the amorphous matrix with the intrinsic ductility of the shape memory phase. During plastic flow, the parent austenite phase undergoes a mechanically-driven diffusion-less transformation in which atoms move cooperatively, often by a shear-like or twin mechanism, to form the martensite phase (i.e., martensitic transformation) [6]. So far, very few MG shape memory composites, mostly based on Ti–Ni, have been reported [7–10] (intermetallic TiNi is one of the most common shape memory alloys [11]). However, because of the low glass forming ability (GFA) of the Ti–Ni system, the wide range of Ti–Ni based shape memory MG composites has been developed only in form of ribbons [7, 8, 12, 13].

In order to fabricate samples with bulk shape, novel MG composites with higher GFA (e.g., based on Cu–Zr) are required. In Cu–Zr based MG composites the shape memory phase also undergoes twinning upon deformation [5]. An effective strategy to enhance the twinning propensity (and promote the martensitic transformation) is to reduce the stacking fault energy (SFE) of the shape memory phase through microalloying [6]. In this sense, partial substitution of Cu with small amounts of Co has been recently reported to reduce the SFE and considerably enhance the plastic deformation of the base alloy (i.e., $Zr_{48}Cu_{48}Al_4$) [6]. Other microalloying elements, such as Ti, V or Ta, do not necessarily improve the mechanical properties of the parent Zr–Cu–Al system [6, 14–16]. For this reason, the effects of varying the Co percentage and/or the influence of microalloying with other elements with small SFE (such as Fe) on the martensitic transformation of Cu–Zr based MG composites is an issue of upmost interest for the structural applications of MG composites and thus requires further investigation.

In this work, a comprehensive study of the influence of varying the concentration of Fe and Co on the microstructure and mechanical performance of $Zr_{48}Cu_{48-x}Al_4M_x$ (M ≡ Fe or Co, $x = 0$, 0.5, 1 at.%) alloys is performed. Our results reveal that addition of small amounts of Fe and Co promotes the martensitic transformation of the parent austenite phase (thus improving plasticity, as expected) but, at the same time, such elements also reduce the GFA of the system. An exceedingly large Fe or Co content (e.g., 1 at.%) increases the amount of crystalline phases significantly, and this is highly detrimental for the resulting plasticity. The amount of Fe and Co in the Zr–Cu–Al system also determines the nature of the crystalline phases as well as twinning propensity. Nanoindentation is used for a detailed study of the mechanically-driven martensitic transformation. Owing to the occurrence of martensitic twins, pop-in events are detected at rather low loads in the loading segments of indentation experiments performed on the austenitic grains. In samples containing Fe or Co, the first pop-in event is observed at lower critical loads, indicating that both microalloying elements promote twinning and the martensitic transformation. Microstructure-dependent variations in hardness and Young's modulus values are also observed and critically depend on the composition.

2. Experimental procedure

Master alloys with a nominal composition of $Zr_{48}Cu_{48-x}Al_4M_x$ (M ≡ Fe or Co, $x = 0$, 0.5, 1 at.%) were prepared by arc melting a mixture of pure elements (>99.9 at.%) in a Zr-gettered high purity argon atmosphere. The master alloys were remelted at least six times to achieve chemically homogeneous ingots. Rod samples of 2 mm in diameter were obtained from the master alloy by copper mould casting in an inert gas atmosphere. The thermal stability was investigated by differential scanning calorimetry (DSC) (Perkin-Elmer DSC-7) at a constant heating rate of 40 K min^{-1}. The structure of the as-cast samples was studied by x-ray diffraction (XRD) (Philips X'Pert) with monochromated Cu K_α radiation (counting time: 7 s, step size: 0.02°). The alloys were chemically etched with 45 ml H_2O, 10 ml HNO_3, and 10 ml HF prior to the microscopy observations. An AxioPlan optical microscope (OM) from Zeiss, a scanning electron microscope (SEM) (Zeiss Merlin), equipped with energy dispersive x-ray (EDX) analysis, and a transmission electron microscope (TEM) (JEM-2011), equipped with selected area electron diffraction (SAED), were used to investigate the microstructure and composition of the alloys. To evaluate the mechanical properties, cylindrical specimens with 2 : 1 aspect

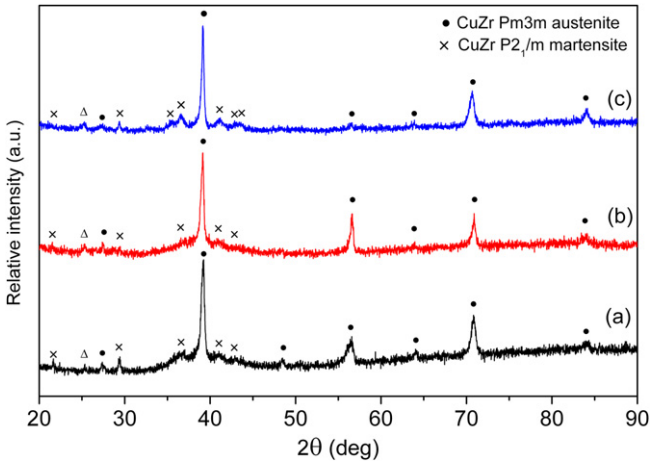

Figure 1. XRD patterns corresponding to (a) $Zr_{48}Cu_{48}Al_4$, (b) $Zr_{48}Cu_{47.5}Al_4Co_{0.5}$ and (c) $Zr_{48}Cu_{47}Al_4Co_1$ as-cast rods. The symbol *Δ* indicates a peak which can neither be assigned to Pm-3m austenite nor to $P2_1/m$ martensite, but its angular position matches the Cm martensite superstructure.

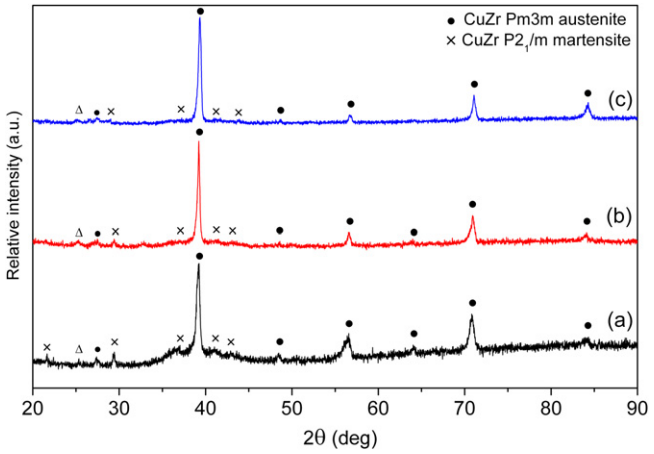

Figure 2. XRD patterns corresponding to (a) $Zr_{48}Cu_{48}Al_4$, (b) $Zr_{48}Cu_{47.5}Al_4Fe_{0.5}$ and (c) $Zr_{48}Cu_{47}Al_4Fe_1$ as-cast rods. The symbol *Δ* indicates a peak which can neither be assigned to Pm-3m austenite nor to $P2_1/m$ martensite, but its angular position matches the Cm martensite superstructure.

ratio were tested at room temperature under compression at a loading rate of $2 \times 10^{-4}\ s^{-1}$ in a universal Servosis machine. Nanoindentation experiments were performed in a UMIS equipment from Fischer-Cripps Laboratories, in the load control mode, at room temperature, on the disks' cross-section, using a diamond Berkovich-type tip. Prior to nanoindentation, the specimens were polished until the surface exhibited a mirror-like appearance. The indentation function consisted of a loading segment of 32 s, to a maximum load of 50 mN, followed by a load holding segment of 20 s and an unloading segment of 32 s. The thermal drift was kept below $0.05\ nm\ s^{-1}$. The hardness (H) and reduced elastic modulus (E_r) values were derived from these load-displacement curves using the method of Oliver and Pharr [17]. The elastic constants were determined using ultrasonic measurements (pulse-echo overlap technique) along with density assessment (Archimedes' method).

3. Results and discussion

3.1. Microstructural and thermal characterization

Figure 1 shows the XRD patterns of the $Zr_{48}Cu_{48}Al_4$, $Zr_{48}Cu_{47.5}Al_4Co_{0.5}$ and $Zr_{48}Cu_{47}Al_4Co_1$ rods. The patterns consist of relatively narrow peaks associated to a crystalline phase superimposed to an amorphous hump detected in the 32°–45° 2θ range. This amorphous halo is clearly visible for $Zr_{48}Cu_{48}Al_4$ but tends to progressively decrease in intensity with the addition of Co. These results suggest that minor additions of Co decrease the GFA of the alloy.

Likewise, partial substitution of Cu by Fe also decreases the GFA of the $Zr_{48}Cu_{48}Al_4$ alloy, as can be deduced from the XRD patterns in figure 2. Actually, Fe appears to have even a larger influence on the decrease of the GFA than Co since only 0.5 at.% Fe addition is enough to make the amorphous halo virtually disappear. The alloy composition is thus of critical importance in determining the resulting microstructure. In fact, similar observations have been made for the ternary Zr–Cu–Al system, without the need a fourth element, where it has been pointed out that small compositional changes (of the order of 1 at.%) can significantly alter the GFA [18]. The microstructure in Zr–Cu–Al alloys can be also tailored by changing the melting current during the casting process, even while keeping the composition constant, hence resulting in highly tunable mechanical properties [19]. The drastic change in microstructure with small compositional variations (of few at.%) is not unique of the Zr–Cu–Al system but has been observed for other MG composites, such as in Mg–Zn–Ca–(Pd) alloys [20].

From the relative intensity of the XRD peaks it can be deduced that the main crystalline phases in the as-cast state are the cubic B2 CuZr austenite (Pm-3m space group, $a = 0.3256$ nm) and the B19′ CuZr martensite ($P2_1/m$ space group). Such phases have been identified using the CaRine v3.1 software [18]. The presence of residual martensite in the as-cast state is somehow anticipated bearing in mind the fabrication process. Namely, the cooling rate is not fast enough for the MG composite to fully retain the stable phase at high temperature (austenite) during suction casting from the liquid. Minor amounts of the martensite superstructure (Cm space group), as proposed by Schryvers *et al* [21], could also be present in the as-cast samples. Evidence for this phase stems from the occurrence of the peak located at around 26° (indicated in figure 1 with the symbol *Δ*), which does not overlap with any of the diffraction peaks from the B2 and B19′ structures. However, it is difficult to unambiguously ascertain the presence of the superstructure phase since most of its diffraction peaks overlap with those of the basic martensite B19′ structure. Interestingly, the amount of martensite phase in the sample containing 1 at.% Co is higher than for 1 at.% Fe. This is consistent with the slightly lower SFE of the B2-CuZr phase when Cu is partially replaced by Co than when it is substituted with Fe [22].

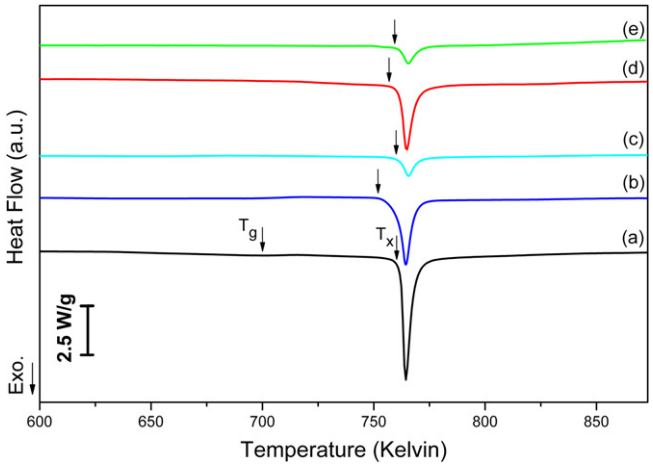

Figure 3. DSC curves corresponding to (a) $Zr_{48}Cu_{48}Al_4$, (b) $Zr_{48}Cu_{47.5}Al_4Co_{0.5}$, (c) $Zr_{48}Cu_{47}Al_4Co_1$, (d) $Zr_{48}Cu_{47.5}Al_4Fe_{0.5}$ and (e) $Zr_{48}Cu_{47}Al_4Fe_1$ as-cast rods.

In order to study the thermal behavior, DSC measurements were carried out for all the compositions (figure 3). All the alloys exhibit one exothermic peak corresponding to the crystallization of the amorphous fraction present in the as-cast sample. The glass transition (T_g) and crystallization (T_x) temperatures for $Zr_{48}Cu_{48}Al_4$ are 703 and 760 K, respectively, rendering a supercooled liquid region of 57 K, similar to other Zr-Cu-Al alloys [23, 24]. The value of T_x practically does not change with increasing the content of Co or Fe while T_g is almost not detectable probably due to the exceedingly small volume fraction of the amorphous counterpart.

The crystallization enthalpy (ΔH) for each composition was evaluated by integrating the area under the exothermic peak (figure 3). For the $Zr_{48}Cu_{48}Al_4$ alloy $\Delta H = 82.4\ J\ g^{-1}$, the highest amongst all the investigated compositions. The values of ΔH decrease when increasing the concentration of Co or Fe. Partial substitution of 0.5 at.% Cu by Co and Fe decreases ΔH to $61.9\ J\ g^{-1}$ and $37.5\ J\ g^{-1}$, respectively. A further decrease of ΔH is obtained for 1 at.% Co (i.e., $17.9\ J\ g^{-1}$) and 1 at.% Fe (i.e., $15.3\ J\ g^{-1}$). The decrease of ΔH is consistent with the decrease in volume fraction of the amorphous fraction with the incorporation of Co or Fe in the Cu–Zr–Al system, as evidenced by XRD (figures 1 and 2).

The microstructure of the $Zr_{48}Cu_{48-x}Al_4M_x$ ($M \equiv$ Fe or Co, $x = 0$, 0.5, 1 at.%) rods was also studied by OM and SEM. The OM images in figures 4(a)–(c) show that the microstructure of $Zr_{48}Cu_{48}Al_4$, $Zr_{48}Cu_{47.5}Al_4Co_{0.5}$ and $Zr_{48}Cu_{47.5}Al_4Fe_{0.5}$ is similar in all cases and consists of second phase particles with rounded shapes embedded in a featureless matrix (i.e., amorphous region). The size and distribution of these particles along the radius of the rod is not uniform, in agreement with what has been observed in other Cu–Zr composites [19]. Namely, the size of the particles tends to be more refined towards the outer region of the rod because of the higher cooling rate achieved during the suction casting process. According to EDX analysis, the crystalline particles in the three alloys contain similar amounts of Cu and Zr and are depleted in Al as compared to the nominal composition. Some of the smaller particles contain a Cu-rich star-

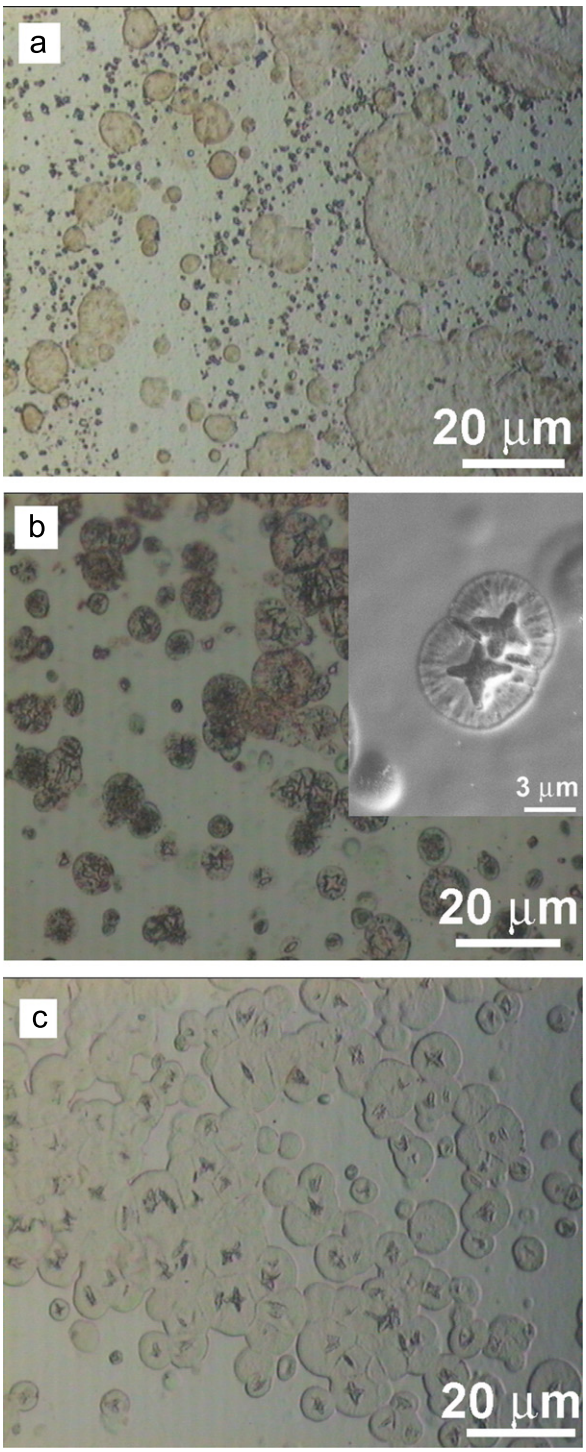

Figure 4. Optical micrographs of the (a) $Zr_{48}Cu_{48}Al_4$ (b) $Zr_{48}Cu_{47.5}Al_4Co_{0.5}$ and (c) $Zr_{48}Cu_{47.5}Al_4Fe_{0.5}$ as-cast rods.

shaped nucleus, with an average atomic composition $Zr_{37}Cu_{60.7}Al_{2.3}$, surrounded by a radial structure, richer in Zr (i.e., $Zr_{50}Cu_{46}Al_4$) than the nominal composition. The resulting average composition of these small particles (including the star-shaped nucleus and the radial region) is, however, slightly richer in Cu than the glassy matrix. The presence of Fe and Co is detected both in the particles and the matrix although their concentration is close to the sensitivity of the EDX technique.

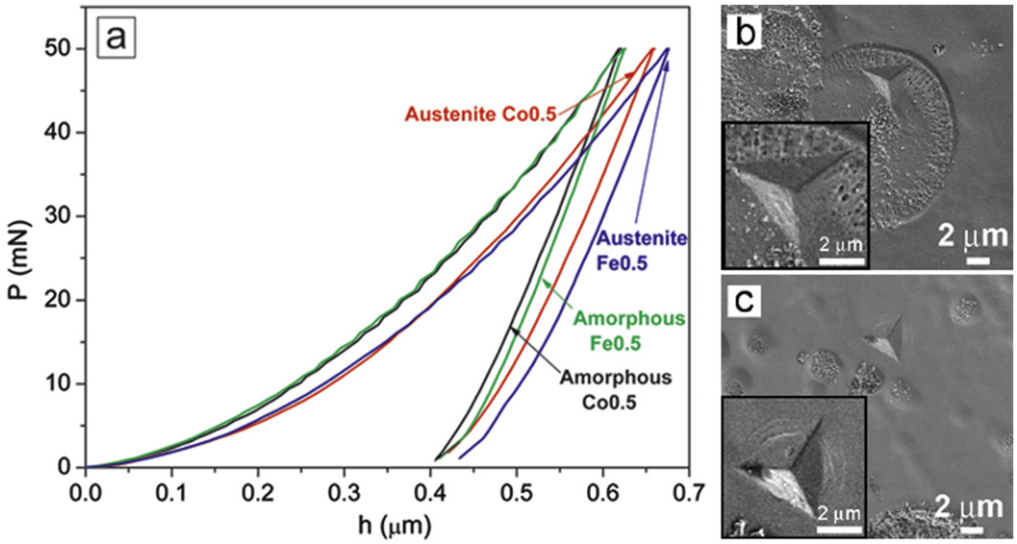

Figure 5. (a) Load-displacement nanoindentation curves performed on the austenite phase and amorphous matrix of the $Zr_{48}Cu_{47.5}Al_4Co_{0.5}$ and $Zr_{48}Cu_{47.5}Al_4Fe_{0.5}$ alloys. SEM images of the indentation impressions performed on the $Zr_{48}Cu_{47.5}Al_4Co_{0.5}$ alloy are shown in (b) for the austenitic phase and (c) for the amorphous matrix.

3.2. Nanoindentation tests

To understand the role of the amorphous and crystalline phases on the mechanical properties, the samples were studied by nanoindentation. Figure 5(a) shows the load-displacement nanoindentation curves obtained from the amorphous matrix and the austenitic phase of the $Zr_{48}Cu_{47.5}Al_4Co_{0.5}$ and $Zr_{48}Cu_{47.5}Al_4Fe_{0.5}$ samples. The curves corresponding to the amorphous regions are very similar in both samples and practically overlap, indicating that the small compositional difference does not have a pronounced influence on the mechanical performance of the glassy matrix. The indentation curves from the austenitic phase of both samples show larger maximum displacement h_{max} values, suggesting that the austenitic phase is softer than the surrounding amorphous matrix. For this reason, for the same maximum stress (i.e., 50 mN), the size of the indent made on austenite (figure 5(b)) is slightly larger than that on the amorphous region (figure 5(c)).

The SEM images also reveal that a large number of shear bands form in the amorphous matrix during nanoindentation. These shear bands are responsible for the pop-in events observed in the loading segments of the nanoindentation curves [2]. Less noticeable and numerous are the shear bands observed for the austenitic phase, which are mainly concentrated inside the indent (figure 5(b)). This is consistent with the smaller shear bursts and smaller number of pop-ins detected on the loading part of the indentation curve in this case. Remarkably, formation of pop-ins during nanoindentation of austenite phases has been reported by other authors [25–27] and are ascribed to twinning and the stress-induced martensitic transformation.

Table 1 lists the values of reduced elastic modulus (E_r), hardness (H) and maximum indentation depth (h_{max}) for the amorphous and crystalline regions of the $Zr_{48}Cu_{48-x}Al_4M_x$ (M ≡ Fe or Co, $x = 0$, 0.5, 1 at.%) alloys. The values of these parameters for the amorphous regions do not significantly change with composition (e.g., H ranges from 8.1 to 9 GPa and E_r from 101 GPa to 113 GPa, i.e., close to 108.2 GPa, as reported by Wu *et al* [28]). Smaller values of H and E_r are obtained in the austenite phase as compared to the amorphous regions of the same alloy. In this case, slight variations are observed, particularly in hardness, depending on the composition. Namely, the smallest value of H corresponds to $Zr_{48}Cu_{48}Al_4$ (i.e., $H = 5.6$ GPa), but addition of 0.5 at.% Co or 0.5 at.% Fe increases H to 7.4 GPa and 7.1 GPa, respectively. Further addition of Co or Fe (1 at.%) results in a slight decrease of H, but the values remain higher than those of the $Zr_{48}Cu_{48}Al_4$ alloy.

It is well known that austenitic phases can undergo martensitic transformations at room temperature under application of mechanical stress. This effect has been reported both in pure elements [29] as well as in austenitic alloys [11]. The mechanically-driven martensitic transformation is related to the propensity for twinning, which in turn depends on the SFE. Since martensite is mechanically harder than austenite, the larger hardness observed for the alloys containing Fe or Co suggests that the amount of martensite, generated during the course of nanoindentation experiments, is larger for these compositions than for $Zr_{48}Cu_{48}Al_4$. Actually, according to the recent work by Zhou *et al* [22], the SFE of B2-CuZr phase along the (011) [100] slip system decreases when increasing the Co content in the stacking fault plane, from 381 mJ m^{-2} (0 at.% Co) to 281 mJ m^{-2} (12.5 at.% Co).

Further insight on the martensitic transformation during nanoindentation was obtained from a detailed analysis of the first pop-in event in the loading segments of nanoindentation curves, performed on the austenitic regions of the different investigated alloys. Figure 6 shows the first pop-in in the load-displacement nanoindentation curves for an amorphous region of the $Zr_{48}Cu_{48}Al_4$ sample and for the austenitic phases of the alloys with $x = 0$, 0.5 and 1. In the latter, the

Table 1. Summary of the values of reduced elastic modulus (E_r), hardness (H) and maximum indentation depth (h_{max}) of the amorphous and crystalline phases corresponding to the $Zr_{48}Cu_{48}Al_4$, $Zr_{48}Cu_{47.5}Al_4Co_{0.5}$, $Zr_{48}Cu_{47}Al_4Co_1$, $Zr_{48}Cu_{47.5}Al_4Fe_{0.5}$ and $Zr_{48}Cu_{47}Al_4Fe_1$ as-cast alloys indented to a maximum load of 50 mN.

Sample	Phase	E_r (GPa)	H (HV)	h_{max} (μm)
$Zr_{48}Cu_{48}Al_4$	Amorphous	112.5 ± 2.4	8.1 ± 0.5	0.62 ± 0.01
	Austenite	87.9 ± 2.5	5.6 ± 0.4	0.76 ± 0.03
$Zr_{48}Cu_{47.5}Al_4Co_{0.5}$	Amorphous	100.6 ± 2.5	8.4 ± 0.1	0.62 ± 0.01
	Austenite	96.9 ± 0.8	7.4 ± 0.7	0.66 ± 0.03
$Zr_{48}Cu_{47}Al_4Co_1$	Amorphous	112.9 ± 2.8	8.7 ± 0.3	0.62 ± 0.01
	Austenite	93.7 ± 0.7	6.5 ± 0.1	0.72 ± 0.01
$Zr_{48}Cu_{47.5}Al_4Fe_{0.5}$	Amorphous	105.4 ± 1.3	8.1 ± 0.1	0.62 ± 0.01
	Austenite	97.8 ± 0.8	7.0 ± 0.5	0.69 ± 0.02
$Zr_{48}Cu_{47}Al_4Fe_1$	Amorphous	107.6 ± 5.0	9.0 ± 2.1	0.61 ± 0.05
	Austenite	92.8 ± 2.6	6.1 ± 0.4	0.75 ± 0.08

stress at which the first pop-in occurs is associated with the onset of the martensitic transformation [27]. Table 2 lists the mean value of the load corresponding to the first pop-in event for $Zr_{48}Cu_{48-x}Al_4M_x$ (M ≡ Co or Fe, $x = 0$, 0.5, 1 at.%) when a maximum load of 1 mN is applied. The dispersion of results (i.e., error bar) is due to the influence of different parameters, such as the crystal orientation, grain size [30] or distance from the grain boundaries [31], which can affect the twinning propensity. The first pop-in load of the austenite phase of the $Zr_{48}Cu_{48}Al_4$ alloy is detected at about 0.18 mN, much earlier than the first pop-in event observed in the amorphous regions of all samples (related to shear band activity). Small additions of Co or Fe are enough to induce significant changes in the value of this critical load. Namely, for 0.5 at.% Co and Fe the critical load decreases from 0.18 mN to 0.09 and 0.12 mN, respectively, hence confirming that these elements enhance the propensity for twinning. These results are reliable in the sense that the size of the indented grains is very similar for all the compositions and, thus, the stress required to induce the martensitic transformation is not influenced by differences in the grain size. Moreover, the grains are very large (micron size), as compared to the nanometer critical grain size below which twinning becomes unlikely to occur in B2 CuZr [30, 32].

3.3. Compression tests

Figure 7 shows the true stress–strain curves for the alloys compressed at room temperature at a strain rate of $2 \times 10^{-4}\ s^{-1}$. All the samples work-harden and finally fail when the ultimate strength is reached. The yield stress, calculated at 0.2% plastic deformation, and the compressive plasticity change with the composition. The base alloy, $Zr_{48}Cu_{48}Al_4$, yields around 1600 MPa, and deforms plastically to about 0.9% before failing at 1870 MPa. The yield stress slightly decreases to 1550 MPa with partial substitution of Cu by 0.5 at.% Co but it increases to 1670 MPa for 1 at.% Co. Conversely, the plastic deformation shows the opposite behavior, i.e., it is maximum for 0.5 at.% Co (about 5.5%) and it decreases to 0.8% for 1 at.% Co. The evolution of the compressive plasticity shows a similar trend in the alloys containing Fe. A maximum compressive plasticity of 6.2% is attained for 0.5 at.% Fe. However, contrary to the alloys with Co, the yield stress in the $Zr_{48}Cu_{48-x}Al_4Fe_x$ alloys decreases gradually as the Fe content is increased, from 1390 MPa (for $x = 0.5$) to 1355 MPa (for $x = 1$).

The change of yield stress and plastic deformation with the composition can be explained from the interplay between several factors: co-existence of the amorphous and crystalline counterparts; nature of the crystalline phase in the as-cast condition (i.e., austenite versus martensite percentage); the propensity for the mechanically-driven martensitic transformation of the pristine austenite phase; and the tendency for deformation-induced nanocrystallization inside shear bands operating in the amorphous matrix.

From the relative intensity of the XRD peaks (figures 1 and 2), it is clear that the amount of martensitic phases with respect to austenite in the as-cast state is larger for the $Zr_{48}Cu_{47}Al_4Co_1$ than for all the other compositions. Considering that the hardness is related to the yield stress through the equation $H = 3\ \sigma_y$ [33], this probably explains why the yield stress for this sample is the highest amongst all the studied alloys. Conversely, the yield stress for $Zr_{48}Cu_{47}Al_4Fe_1$ is the smallest among all the compositions probably because the volume fraction of martensite phases is also the lowest in this case (figure 2).

Taking into account the microstructure of the alloys, the large plasticity of $Zr_{48}Cu_{47.5}Al_4Co_{0.5}$ and $Zr_{48}Cu_{47.5}Al_4Fe_{0.5}$ could be due to various effects: (i) the role of the crystalline particles in promoting nucleation and branching of the shear bands activated within the amorphous matrix, which depends on the size of the crystalline particles and the presence or not of the glassy matrix [34]; (ii) the phase transformation of the crystalline particles, from austenite to martensite, during the course of compression experiments [35]; (iii) eventual deformation-induced nanocrystallization inside shear bands [2, 36]. In MG composites being deformed in the plastic regime, the presence of the ductile crystalline particles embedded in the amorphous matrix facilitates the multiplication of shear bands at the amorphous/crystal interface due to the difference in the Young's modulus values between the glassy and crystalline regions [2]. The composition of the amorphous matrix (and thus its thermal stability and mechanical properties) is similar for all samples; therefore no

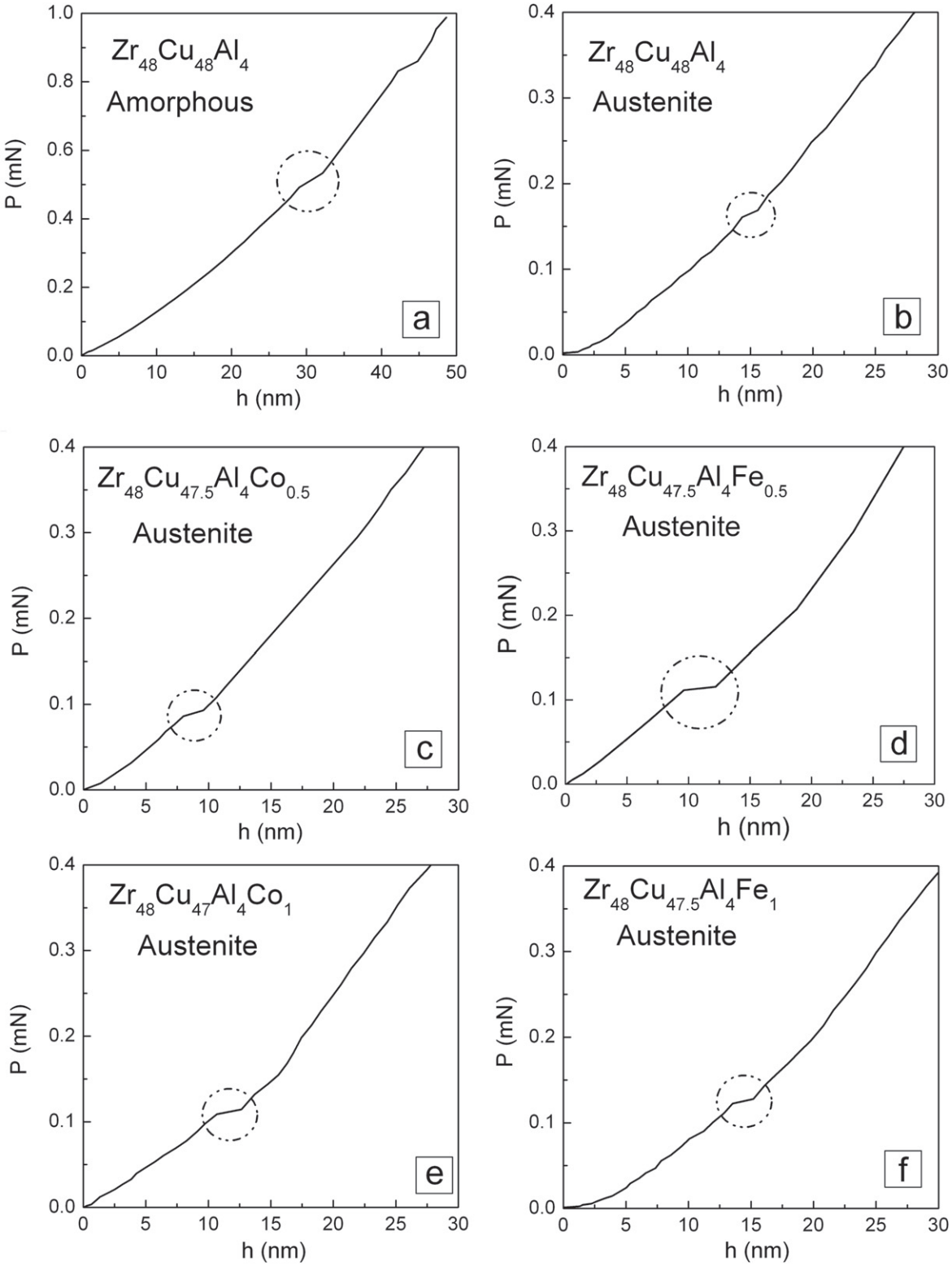

Figure 6. First pop-in event observed in the load-displacement nanoindentation curves corresponding to (a) the amorphous matrix of sample $Zr_{48}Cu_{48}Al_4$, (b) the austenite phase in $Zr_{48}Cu_{48}Al_4$, (c) the austenite phase in $Zr_{48}Cu_{47.5}Al_4Co_{0.5}$, (d) the austenite phase in $Zr_{48}Cu_{47.5}Al_4Fe_{0.5}$, (e) the austenite phase in $Zr_{48}Cu_{47}Al_4Co_1$ and (f) the austenite phase in $Zr_{48}Cu_{47}Al_4Fe_1$.

pronounced differences in the nanocrystallization within shear bands should be expected depending on x. Thus, factors (i) and (ii) are probably the main ones governing the high plasticity observed in the $Zr_{48}Cu_{47.5}Al_4M_{0.5}$ alloys. The shear bands nucleated in the amorphous regions can freely propagate until they encounter an austenite crystal [37]. Since this phase is rather ductile, it can easily accommodate the strain, while undergoing a martensitic transformation and

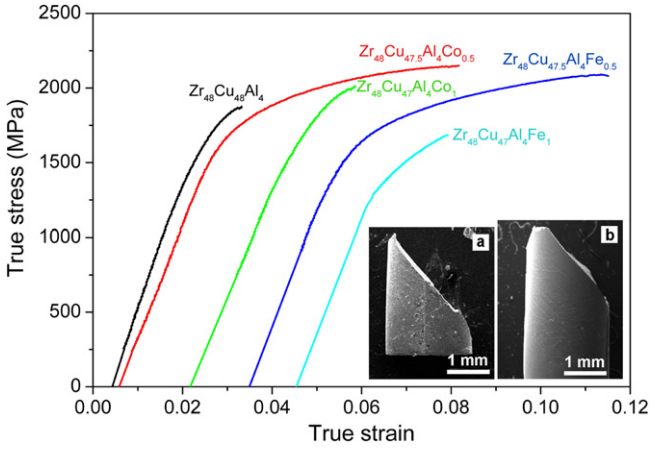

Figure 7. Compressive stress–strain curves for the $Zr_{48}Cu_{48}Al_4$, $Zr_{48}Cu_{47.5}Al_4Co_{0.5}$, $Zr_{48}Cu_{47}Al_4Co_1$, $Zr_{48}Cu_{47.5}Al_4Fe_{0.5}$ and $Zr_{48}Cu_{47}Al_4Fe_1$ as-cast rods. The insets are optical micrographs showing the fracture angle for (a) $Zr_{48}Cu_{47.5}Al_4Co_{0.5}$ and (b) $Zr_{48}Cu_{47.5}Al_4Fe_{0.5}$ rods. The compression curves have been shifted horizontally for the sake of clarity.

Table 2. Critical load, P_c, corresponding to the first pop-in event in the load-displacement nanoindentation curves of the different investigated samples.

Max. load 1 mN	P_c (mN)
$Zr_{48}Cu_{48}Al_4$ (austenite)	0.18 ± 0.03
$Zr_{48}Cu_{47.5}Al_4Co_{0.5}$ (austenite)	0.09 ± 0.02
$Zr_{48}Cu_{47}Al_4Co_1$ (austenite)	0.11 ± 0.02
$Zr_{48}Cu_{47.5}Al_4Fe_{0.5}$ (austenite)	0.12 ± 0.03
$Zr_{48}Cu_{47}Al_4Fe_1$ (austenite)	0.13 ± 0.03
$Zr_{48}Cu_{48}Al_4$ (amorphous)	0.56 ± 0.05

consequently becoming harder than the undeformed regions. Hence, the martensitic transformation is responsible for the observed work-hardening effect.

Microalloying with Co or Fe presumably decreases the SFE of CuZr Pm-3m austenite (as evidenced from nanoindentation, table 2, and in agreement with recent theoretical calculations [6, 22]), thus facilitating deformation twinning and the phase transformation from austenite to martensite when the alloys are subjected to stress (i.e., factor (ii)) [6]. However, the decrease of plasticity for samples with $x = 1$, compared to the alloys with $x = 0.5$, cannot be easily explained simply in terms of the martensitic transformation. Austenite (whose amount is maximized for $Zr_{48}Cu_{47}Al_4Fe_1$) is more prone to plastic deformation than the martensite phase or the amorphous regions [38]. Nevertheless, $Zr_{48}Cu_{47}Al_4Fe_1$ shows rather limited plastic flow. In turn, the compressive plasticity for $Zr_{48}Cu_{47}Al_4Co_1$ is similar to that of the $Zr_{48}Cu_{48}Al_4$ base alloy, which has higher volume fraction of austenite but also larger volume fraction of amorphous matrix. Our results indicate that although minor alloying with elements of similar electronegativity and atomic size as Cu and Zr in the B2 phase indeed promotes the martensitic transformation (factor (ii)) [6], an excess addition of these alloying elements drastically decreases the plasticity. Remarkably, a non-monotonic dependence of the compressive plasticity with the Co content in Zr–Cu–Al alloys has been reported by other authors recently [16], although the theoretical studies predict a progressive decrease of the SFE with the increase of the Co content inside the stacking fault plane [22]. Such apparent discrepancy can be understood bearing in mind that addition of Co and Fe significantly reduces the GFA (as evidenced from XRD and DSC results, thus influencing factor (i)). The presence of both, the austenite phase and the amorphous matrix, is necessary to attain large plasticity. Actually, monolithic polycrystalline austenite rods (with no glassy matrix) have been reported to exhibit lower plastic strain than MG composites [19], where the austenite grains can hinder the catastrophic rapid propagation of the shear bands nucleated in the glassy matrix, while causing their multiplication and increasing the plasticity. Actually, recent studies on Zr–Cu–Al alloys prepared using different melting currents (a procedure which allows tailoring the microstructure without varying the composition), have shown that the plasticity is maximum for an austenite volume fraction around 30%, but it decreases for larger austenite contents [19]. Moreover, the presence of martensite phase in the as-cast state (for example in $Zr_{48}Cu_{47}Al_4Co_1$) also contributes to decrease the overall plasticity, since this phase is more brittle than the austenite [39].

The samples with largest compressive plasticity were observed by optical microscopy (insets of figure 7) to better understand the failure mechanism under compression. The fracture angle of the $Zr_{48}Cu_{47.5}Al_4Co_{0.5}$ and $Zr_{48}Cu_{47.5}Al_4Fe_{0.5}$ rods (insets of figures 7(a) and (b) respectively) is about 40°–42° with respect to the loading axis, hence lower than 45° as it would be expected for a polycrystalline material following the von Mises yield criterion [40]. This indicates that the alloys exhibit a pressure-dependent yield behavior. This result is consistent with the fracture angle observed in most MGs such as in Zr–Ti–Ni–Cu–Be (i.e., ~40°) [41, 42] and $Zr_{59}Cu_{20}Al_{10}Ni_8Ti_3$ (i.e., 43°) [43] or some MG composites [44]. Small additions of Co and Fe do not have an influence on the pressure dependence since the fracture angle for the five compositions is practically the same. The SEM observations of the compressed specimens (not shown) also reveal the occurrence of a high number of shear offsets at the lateral surfaces of the rods, especially for the $Zr_{48}Cu_{47.5}Al_4Fe_{0.5}$ alloy, which exhibits the maximum plasticity. The primary and secondary shear bands generated during compression can interact with each other during their propagation, thus favoring plastic deformation [45].

To further confirm the role of the stress-induced martensitic transformation on the mechanical performance, the rods were cut into slices of about 0.5 mm in thickness, subsequently compressed to 2100 MPa for 4 min and finally characterized by XRD, to assess the deformation-induced structural changes. The compression conditions were chosen so that the duration of these tests is similar to the macroscopic compression tests shown in figure 7 but, due to the shorter length of these specimens, premature fracture was avoided. These conditions are the same for all the compositions to better assess the susceptibility for the martensitic

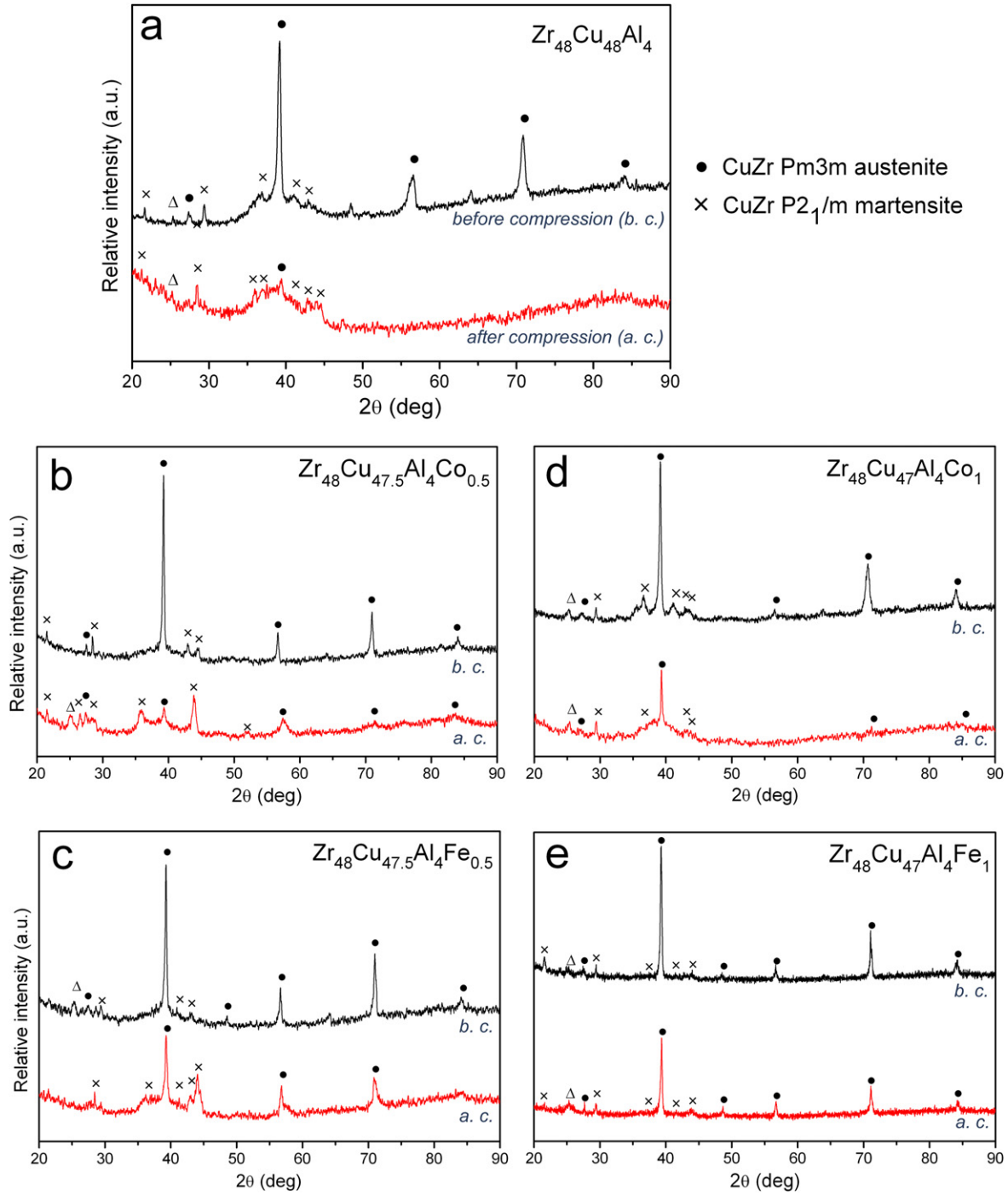

Figure 8. XRD patterns acquired before and after compression experiments corresponding to (a) $Zr_{48}Cu_{48}Al_4$, (b) $Zr_{48}Cu_{47.5}Al_4Co_{0.5}$, (c) $Zr_{48}Cu_{47.5}Al_4Fe_{0.5}$, (d) $Zr_{48}Cu_{47}Al_4Co_1$ and (e) $Zr_{48}Cu_{47}Al_4Fe_1$. The symbol Δ indicates a peak which can neither be assigned to Pm-3m austenite nor to P2$_1$/m martensite, but its angular position matches the Cm martensite superstructure.

transformation. The XRD patterns of the slices before and after the compression tests are shown in figure 8. For the $Zr_{48}Cu_{48}Al_4$ alloy, most of the XRD peaks corresponding to austenite disappear after compression, while the intense austenite peak located at 39° tends to become partly overlapped with the amorphous hump (figure 8(a)). Concurrently, the intensity of the martensite peaks increases, as a consequence of the mechanically-driven martensitic transformation. Interestingly, the wide hump in the angular range 32°–45° also becomes more visible after compression, indicating that the stress generated during compression not only induces martensitic transformation but is also responsible for partial distortion of the crystalline lattice, which is consistent with the results by Wu *et al* for this type of alloys [34]. The XRD patterns of $Zr_{48}Cu_{47.5}Al_4Co_{0.5}$ (figure 8(b)) and $Zr_{48}Cu_{47.5}Al_4Fe_{0.5}$ (figure 8(c)) alloys after compression are rather similar. For both compositions the relative intensity of the peaks associated to austenite decreases after

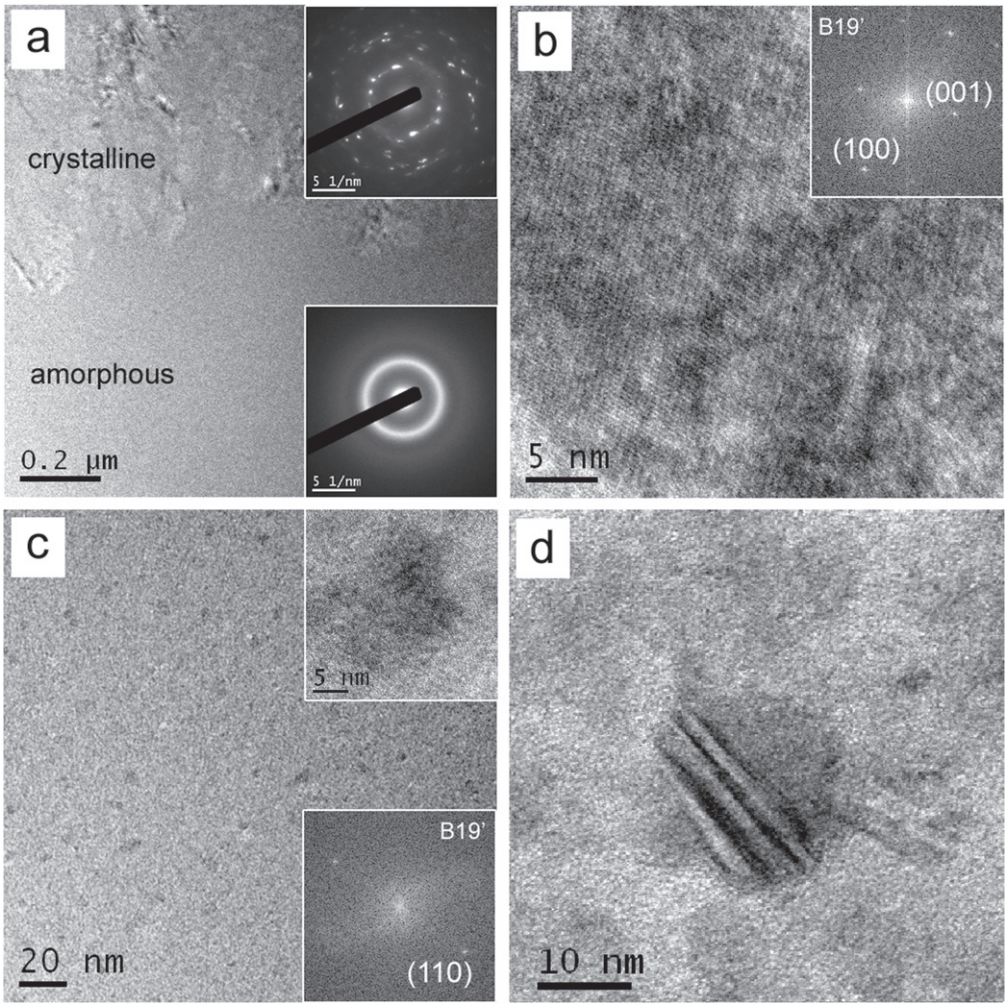

Figure 9. TEM images of the $Zr_{48}Cu_{47.5}Al_4Co_{0.5}$ alloy compressed to 2100 MPa for 4 min. Panel (a) shows the boundary between a crystalline globular region and the surrounding amorphous matrix, with the corresponding SAED patterns shown as insets. Panel (b) is a high-resolution TEM image obtained inside a crystalline globular region. Panel (c) is a high-resolution TEM image of the amorphous-like matrix. Panel (d) shows an example of intragranular nanotwins.

compression while the intensity of the peaks corresponding to martensite increases. A wide amorphous hump is also detected but its intensity is smaller than for $Zr_{48}Cu_{48}Al_4$ alloy, suggesting that the compressive energy has been used, to a large extent, to induce the martensitic transformation. Nevertheless, the austenite peaks for the $Zr_{48}Cu_{47.5}Al_4M_{0.5}$ alloys also tend to become wider after compression, indicating that austenite not only undergoes a stress-induced martensitic transformation but its crystalline lattice becomes distorted during the mechanical deformation. Similar phase transformations occur for samples with $x = 1$ (figures 8(d) and (e)), although no clear amorphous hump is generated for 1 at.% Fe, probably because of the rather low GFA of this alloy.

Evidence for the deformation-induced martensitic transformation and the occurrence of intragranular nanotwins was obtained by TEM. Representative TEM images of the $Zr_{48}Cu_{47.5}Al_4Co_{0.5}$ alloy compressed to 2100 MPa for 4 min are shown in figure 9. Figure 9(a) shows the boundary between a glassy and a globular crystalline region (in agreement with the microstructure observed by optical microscopy, i.e., figure 4).

While no clear spots or crystalline rings are obtained in the SAED pattern of the amorphous matrix (bottom inset in panel 9(a)), various spots revealing coexistence of the B2 (austenite) and B19′ (martensite) phases are identified in the SAED pattern corresponding to the crystalline globular region (upper inset in panel 9(a)). An example of a high-resolution TEM image, acquired inside one of the globular crystalline regions, is shown in figure 9(b). In this case, the interplanar distance matches that of the {100} planes of the B19′ phase.

Interestingly, very small crystallites, also corresponding to B19′ martensite, with sizes often smaller than 10 nm, are observed in the high-magnification image of the glassy matrix (figure 9(c)). Some of these crystals (particularly those with sizes around 10–20 nm) contain intragranular nanotwins, probably generated during the course of the compression experiments (figure 9(d)). It is believed that these nanotwins are generated from the austenite phase and act as nucleation sites of the martensite phase [6]. Further examples of these

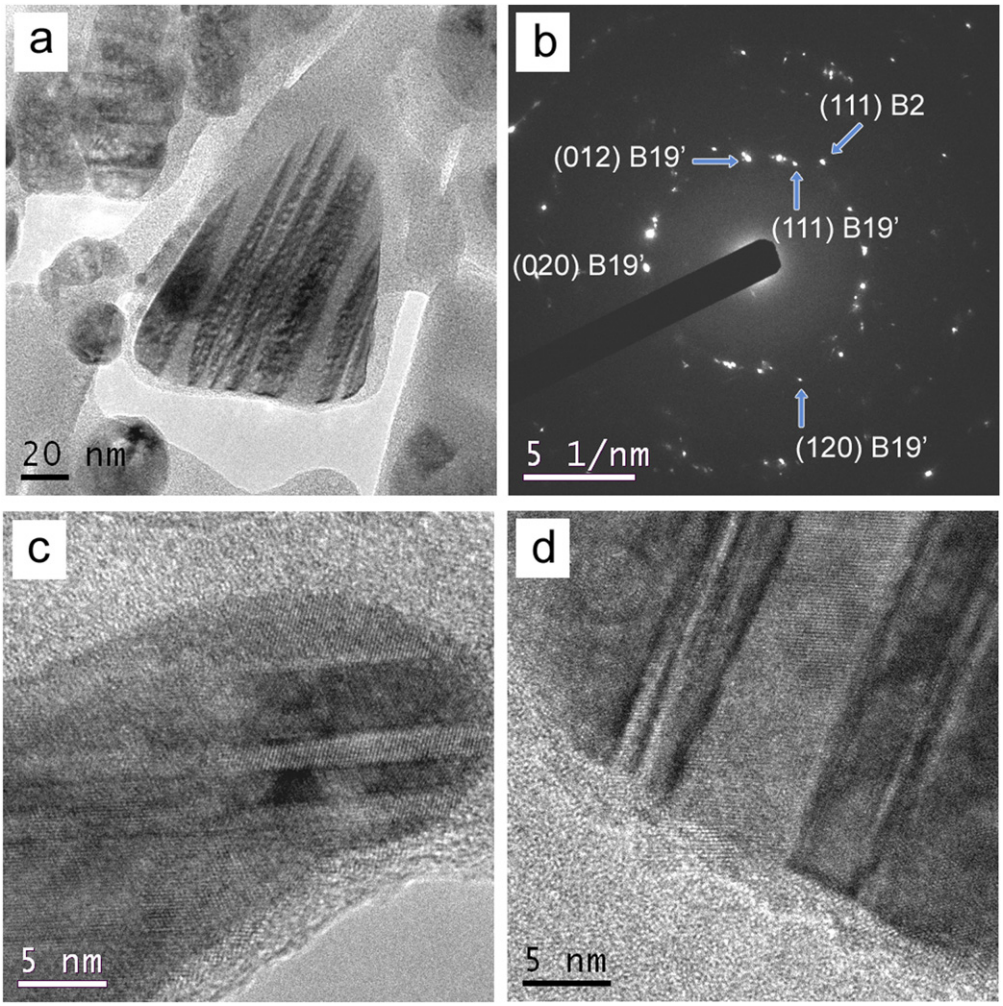

Figure 10. TEM images of the $Zr_{48}Cu_{47.5}Al_4Fe_{0.5}$ alloy compressed to 2100 MPa for 4 min. Panels (a), (c) and (d) show examples of intragranular nanotwins formed inside the crystalline particles during compression. Panel (b) is a SAED pattern of these crystals, revealing the coexistence of B2 (austenite) and B19′ (martensite) phases.

Table 3. Summary of the elastic properties determined from acoustic measurements on the as-cast samples at room temperature: Poisson's ratio (ν), shear modulus (G), bulk modulus (B) and Young's modulus (E).

Alloy composition	ν	G (GPa)	B (GPa)	E: acoustic measurements (GPa)
$Zr_{48}Cu_{48}Al_4$	0.368	33.2 ± 0.5	114.6 ± 0.5	90.8 ± 0.5
$Zr_{48}Cu_{47.5}Al_4Co_{0.5}$	0.375	31.4 ± 0.5	115.4 ± 0.5	86.3 ± 0.5
$Zr_{48}Cu_{47}Al_4Co_1$	0.369	33.7 ± 0.5	118.1 ± 0.5	92.4 ± 0.5
$Zr_{48}ACu_{47.5}Al_4Fe_{0.5}$	0.382	31.9 ± 0.5	124.8 ± 0.5	88.1 ± 0.5
$Zr_{48}Cu_{47}Al_4Fe_1$	0.376	31.2 ± 0.5	115.3 ± 0.5	85.9 ± 0.5

nanotwins are shown in figure 10, which provides the results of TEM observations on the compressed $Zr_{48}Cu_{47.5}Al_4Fe_{0.5}$ specimen. The SAED pattern of an ensemble of these crystallites reveals coexistence of austenite and martensite phases (in agreement with the XRD pattern in figure 8(c)). Several intragranular nanotwins are often generated inside many of the crystals (figures 10(a), (c) and (d)). The occurrence of intragranular nanotwins can hinder dislocation motion through the twin boundaries, thus enhancing hardness by a dislocation pile-up mechanism similar what it often occurs at grain boundaries [46].

3.4. Acoustic measurements

Table 3 summarizes the values of elastic properties, i. e. Poisson's ratio (ν), shear modulus (G), bulk modulus (B) and Young's modulus (E), obtained from acoustic measurements on the $Zr_{48}Cu_{48-x}Al_4Co_x$ and $Zr_{48}Cu_{48-x}Al_4Fe_x$ ($x = 0$, 0.5 and 1) as-cast alloys. The observed differences as a function of composition can be mainly ascribed to the different volume fractions of the phases constituting the alloys since the elastic constants of austenite, martensite and amorphous counterparts are different. For example, the value of E for B2 CuZr is about 82 GPa [19, 25, 47] smaller than for the corresponding

Table 4. Summary of the elastic properties determined from acoustic measurements on the samples after the compression tests, at room temperature, to 2100 MPa for 4 min: Poisson's ratio (ν), shear modulus (G), bulk modulus (B) and Young's modulus (E).

Alloy composition	ν	G (GPa)	B (GPa)	E: acoustic measurements (GPa)
$Zr_{48}Cu_{48}Al_4$	0.369	33.4 ± 0.5	116.5 ± 0.5	91.5 ± 0.5
$Zr_{48}Cu_{47.5}Al_4Co_{0.5}$	0.377	33.3 ± 0.5	124.0 ± 0.5	91.7 ± 0.5
$Zr_{48}Cu_{47}Al_4Co_1$	0.364	34.8 ± 0.5	116.5 ± 0.5	95.1 ± 0.5
$Zr_{48}ACu_{47.5}Al_4Fe_{0.5}$	0.373	33.9 ± 0.5	121.8 ± 0.5	93.2 ± 0.5
$Zr_{48}Cu_{47}Al_4Fe_1$	0.382	32.2 ± 0.5	125.3 ± 0.5	88.9 ± 0.5

martensite phase (around 110 GPa). In turn, the Young's modulus of the amorphous alloy with analogous composition is slightly higher than that of the B2 austenite phase although smaller than for the martensite, as reported by Pauly *et al* [19]. This is different to what is normally encountered in bulk MGs, where a reduction of E in the glassy structure with respect to the corresponding crystalline counterpart (an effect referred to as 'elastic softening') is observed [47]. Remarkably, acoustic measurements provide the values of Young's modulus not being affected by eventual mechanically-driven martensitic transformations occurring during macroscopic compression or nanoindentation experiments.

In the as-cast samples, the addition of 0.5% Co decreases the Young's modulus of the $Zr_{48}Cu_{48}Al_4$ alloy because the relative volume fraction of amorphous region compared with that of austenite phase decreases. Further addition of Co (1 at.%) results in a slight increase of E due to the higher amount of martensitic phase and lower amount of amorphous region. A similar reasoning explains the trends in E for the samples containing 0.5 at.% and 1 at.% Fe. In this case, however, the $Zr_{48}Cu_{47}Al_4Fe_1$ sample contains lower amount of martensite than $Zr_{48}Cu_{47}Al_4Co_1$ and the Young's modulus is therefore lower. The values of G (33.2 GPa) and B (114.6 GPa) obtained for $Zr_{48}Cu_{48}Al_4$ alloy are similar to those reported in the literature [48]. The Poisson's ratio, indicative of the plasticity of a material [49], lies within the range 0.36–0.37, as reported for Zr–Cu–Al BMGs [50], and increases with the addition of Co or Fe. The maximum value of the Poisson's ratio, $\nu = 0.382$, occurs for 0.5 at.% Fe, for which the maximum compressive plasticity is attained.

The elastic properties of the samples compressed to 2100 MPa for 4 min were also measured (table 4). Comparing these results with those of the as-cast sample (table 3) it is observed that E generally increases after compression, due to the occurrence of the aforementioned martensitic transformation.

4. Conclusions

The microstructure of $Zr_{48}Cu_{48-x}Al_4M_x$ (M ≡ Fe or Co, $x = 0$, 0.5, 1 at.%) alloys consists of B2 CuZr austenite and P21/m martensite crystals embedded in an amorphous matrix, with different phase percentages depending on the exact alloy composition. These alloys undergo a deformation-induced martensitic transformation during compression tests and nanoindentation, which induces variations in the measured values of hardness, Young's modulus, yield stress and compressive plasticity, as well as on the work-hardening behavior. The plasticity, which is usually lacking or very limited in monolithic bulk MGs, is maximized for the alloys with $x = 0.5$ (with a total strain of about 5.5% and 6.2% for 0.5 at.% of Co or Fe, respectively). The propensity for the austenite phase to exhibit a mechanically-driven martensitic transformation depends on the composition and is found to be promoted for the alloys containing Fe or Co. Evidence for this is obtained from nanoindentation, macroscopic compression, XRD and acoustic measurements. In spite of the beneficial effect of adding Fe or Co to the $Zr_{48}Cu_{48}Al_4$ alloy (in terms of promoting the martensitic transformation), these elements also reduce the GFA. The percentage of amorphous matrix drastically decreases for alloys with $x = 1$, as compared to those with $x = 0$ or $x = 0.5$. The large amount of crystalline regions in these samples has a detrimental effect on the resulting compressive plasticity, which is drastically reduced as compared to the alloys with $x = 0.5$. Thus our results indicate that the mechanical performance of the different investigated alloys critically depends on the interplay between several factors: (a) the coexistence of the shape memory crystalline phases and the MG matrix, (b) nature of the crystalline phase in the as-cast condition (i.e., austenite or martensite) and (c) propensity of the austenite to undergo a martensitic transformation (which also depends on the composition). These results are of high interest in order to optimize the microstructure of bulk MG composites to fulfil the technological demands of these materials for structural applications.

Acknowledgements

This work has been partially financed by the 2014-SGR-1015 and MAT2011-27380-C02-01 research projects. SG acknowledges the *Juan de la Cierva* Fellowship from the Spanish Ministry of Science and Innovation. EP is grateful to the Spanish MINECO for the Ramon y Cajal contract (RYC-2012-10839). MDB was partially supported by an ICREA Academia award. We also acknowledge the technical support from Anna Hynowska and Dr Pablo Castro in the sample preparation for TEM observations.

References

[1] Li M, Eckert J, Kecskes L and Lewandowski J 2007 *J. Mater. Res.* **22** 255
[2] Schuh C A, Hufnagel TC and Ramamurty U 2007 *Acta Mater.* **55** 4067
[3] Concustell A, Sort J, Alcalá G, Mato S, Gebert A, Eckert J and Baró M D 2005 *J. Mater. Res.* **20** 2719
[4] van Steenberge N, Sort J, Concustell A, Das J, Scudino S, Suriñach S, Eckert J and Baró M D 2007 *Scr. Mater.* **56** 605
[5] Pauly S, Gorantla S, Wang G, Kühn U and Eckert J 2010 *Nat. Mater.* **9** 473
[6] Wu Y, Zhou D Q, Song W L, Wang H, Zhang Z Y, Ma D, Wang X L and Lu Z P 2012 *Phys. Rev. Lett.* **109** 245506
[7] Rösner H, Schloβmacher P, Shelyakov A V and Glezer A M 2001 *Acta Mater.* **49** 1541
[8] Wang X and Vlassak J J 2006 *Scr. Mater.* **54** 925
[9] Das J, Pauly S, Boström M, Durst K, Göken M and Eckert J 2009 *J. Alloys Compd.* **483** 97
[10] Pieczyska E, Gadaj S, Nowacki WK, Hoshio K, Makino Y and Tobushi H 2005 *Sci. Technol. Adv. Mater.* **6** 889
[11] Otsuka K and Ren X 2005 *Prog. Mater. Sci.* **50** 511
[12] Kang S W, Lee Y H, Lim Y M, Nam J M, Nam T H and Kim Y W 2008 *Scr. Mater.* **59** 1186
[13] Nam T H, Lee J H, Cho G B and Kim Y W 2006 *Mater. Sci. Eng.* A **438-440** 687
[14] Pan J, Li L and Chan K C 2009 *Scr. Mater.* **60** 882
[15] Pan J, Chan K C, Chen Q, Li N, Guo S F and Liu L 2010 *J. Alloys Compd* **504** S74
[16] Kuo C N, Huang J C, Du X H, Liu X J and Nieh T G J 2014 *Alloys Compd* **586** S14
[17] Oliver W C and Pharr G M 1992 *J. Mater. Res.* **7** 1564
[18] Qiu F, Shen P, Liu T, Lin Q and Jiang Q 2010 *J. Alloys Compd.* **491** 354
[19] Pauly S, Liu G, Wang G, Kühn U, Mattern N and Eckert J. 2009 *Acta Mater.* **57** 5445
[20] González S, Pellicer E, Fornell J, Blanquer A, Barrios L I, Ibáñez E, Solsona P, Suriñach S, Baró M D, Nogués C and Sort J 2012 *J. Mech. Behav. Biomed. Mater.* **6** 53
[21] Schryvers D, Firstov G S, Seo J W, Van Humbeeck J and Koval Y N 1997 *Scr. Mater* **36** 1119
[22] Zhou D Q, Wu Y, Wang H, Hui X D, Liu X J and Lu Z P 2013 *Comput. Mater. Sci.* **79** 187
[23] Zhang G Q, Jiang Q K, Chen L Y, Shao M, Liu J F and Jiang J Z 2006 *J. Alloys Compd.* **424** 176
[24] Meng F Q, Tsuchiya K, Yin F X and Yokoyama Y 2012 *J. Alloys Compd.* **522** 136
[25] Caër C, Patoor E, Berbenni S and Lecomte J S 2013 *Mater. Sci. Eng.* A **587** 304
[26] Misra R D K, Zhang Z, Jia Z, Venkat Surya P K C, Somani M C and Karjalainen L P 2011 *Mater. Sci. Eng.* A **528** 6958
[27] Ahn T H, Oh C-S, Kim D H, Oh K H, Bei H, George E P and Han H N 2010 *Scr. Mater.* **63** 540
[28] Wu Y, Xiao Y, Chen G, Liu C T and Lu Z 2010 *Adv. Mater.* **22** 2770
[29] Sort J, Nogués J, Suriñach S and Baró M D 2003 *Phil. Mag.* **83** 439
[30] Pauly S, Liu G, Gorantla S, Wang G, Kühn U, Kim D H and Eckert J 2010 *Acta Mater.* **58** 4883
[31] Ohmura T and Tsuzaki K 2007 *J. Mater. Sci.* **42** 1728
[32] Chen M W, Ma E, Hemker K J, Sheng H, Wang Y M and Cheng X M 2003 *Science* **300** 1275
[33] Marcinkowski M J, Fisher R M and Szirmae A 1964 *Trans. TMS-AIME* **230** 676
[34] Wu Y, Wang H, Wu H H, Zhang Z Y, Hui X D, Chen G L, Ma D, Wang X L and Lu Z P 2011 *Acta Mater.* **59** 2928
[35] Fornell J, Baró M D, Suriñach S, Gebert A and Sort J 2011 *Adv. Eng. Mater.* **13** 57
[36] Chen M, Inoue A, Zhang W and Sakurai T 2006 *Phys. Rev. Lett.* **96** 245502
[37] Ott R T, Sansoz F, Molinari J F, Almer J, Ramesh K T and Hufnagel T C 2005 *Acta Mater.* **53** 1883
[38] Johnson W L 2002 *JOM* **54** 40
[39] Wei R, Chang Y, Li Y F, Li G, Yang S, Zhang C J and He L 2013 *Mater. Sci. Eng.* A **587** 233
[40] Donovan P E 1989 *Acta Mater.* **37** 445
[41] Lewandowski J J and Lowhaphandu P 2002 *Phil. Mag.* A **82** 3427
[42] Fornell J, Concustell A, Suriñach S, Li W H, Cuadrado N, Gebert A, Baró M D and Sort J. 2009 *Int. J. Plasticity* **25** 1540
[43] Zhang Z F, Eckert J and Schultz L 2003 *Acta Mater.* **51** 1167
[44] Zhang Z F, Eckert J and Schultz L 2003 *Phys. Rev. Lett.* **91** 045505
[45] Gonzalez S, Chen N, Zhang QS, Louzguine-Luzgin DV, Perepezko J H and Inoue A. 2011 *Scr. Mater.* **64** 713
[46] Sort J, Zhilyaev A, Zielinskaa M, Nogués J, Suriñach S, Thibault T and Baró M D. 2003 *Acta Mater.* **51** 6385
[47] Gebert A, Wolff U, John A, Eckert J and Schultz L. 2001 *Mater. Sci. Eng.* A **299** 125
[48] Yu P, Bai H Y, Tang M B and Wang W L 2005 *J. Non-Cryst. Solids* **351** 1328
[49] Lewandowski J J, Wang W H and Greer A L. 2005 *Phil. Mag. Lett.* **85** 77
[50] Kumar G, Ohkubo T, Mukai T and Hono K 2007 *Scr. Mater.* **57** 173